Finite-temperature magnetism in amorphous Fe - Y alloys

Finite-temperature magnetism in amorphous Fe–Y alloys

M Yu† and Y Kakehashi

Hokkaido Institute of Technology, Maeda, Teine-ku, Sapporo 006, Japan

Abstract. Various magnetic properties of amorphous Fe–Y alloys at finite temperatures such as the densities of states, local magnetic moments, susceptibilities, and the magnetic phase diagram have been investigated on the basis of the finite-temperature theory of amorphous magnetic alloys. It is found that the calculated magnetization, distribution of local moments, susceptibilities, and magnetic phase diagram in the most random atomic configuration show a spin-glass phase, a re-entrant spin-glass phase, ferromagnetism, and paramagnetism with reducing Fe concentration. These results describe qualitatively the experimental data for the melt-spun Fe–Y alloys. It is verified that the nonlinear magnetic couplings between Fe local moments and the large-amplitude fluctuations of local moments due to structural disorder result in the spin glass in the Fe-rich region. The decrease of the average coordination number of the Fe atom due to the large difference in atomic size between Fe and Y atoms, on the other hand, stabilizes the ferromagnetism at lower Fe concentrations. The difference in magnetic phase diagram between the melt-spun and the sputtered Fe–Y alloys is interpreted in terms of that between the atomic short-range orders.

1. Introduction

The magnetic properties of Fe-rich amorphous alloys containing early transition metals or rare-earth metals have been much investigated experimentally since the beginning of the 1980s [1–13]. Their magnetic phase diagrams have been established as shown in figure 1. These phase diagrams show a characteristic feature of the magnetism: the Curie temperatures rapidly decrease with increasing Fe concentration, and the spin-glass (SG) phase is found beyond 90 at.% Fe. The SG transition temperatures (T_g) obtained take approximately the same value of about 110 K irrespective of the choice of second element. The SG, therefore, is considered to be intrinsic to amorphous pure Fe.

A theory which explains the SG in amorphous pure Fe has been presented by Kakehashi on the basis of the functional integral method and the distribution function method [14]. He showed that the SG in amorphous Fe is caused by nonlinear magnetic couplings between Fe local moments (LMs) and the large fluctuations of the amplitude of LMs due to structural disorder. This feature has recently been examined in more detail by varying the volume [15] and the degree of structural disorder [16], and even by improving the theory in such a way that the amplitude fluctuations on the nearest-neighbour (NN) shell are selfconsistently taken into account [17].

When the Fe concentration is decreased, the phase diagrams in figure 1 show common features: the SG phase beyond 90 at.% Fe, the re-entrant spin-glass (RSG) behaviour,

---

† E-mail: yum@audrey.mpi-stuttgart.mpg.de; present address: Max-Planck-Institut für Physik Komplexer Systeme, Heisenbergstrasse 1, Postfach 800665, D-70506 Stuttgart, Germany.
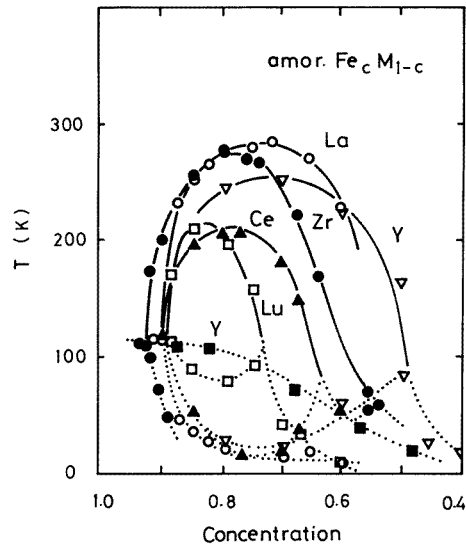
Figure 1. Magnetic phase diagrams of Fe-rich amorphous alloys containing the early transition metals and rare-earth metals. The Curie (spin-glass transition) temperatures are shown by solid (dashed) curves. The data for amorphous Fe–Lu (□), Fe–Ce (▲), Fe–Zr (●), and Fe–La (○) are taken from [11, 13], while the data for amorphous Fe–Y (melt-spun: ▽; sputtered: ■) are taken from [1] and [5], respectively.

the appearance of ferromagnetism (F), and the transition to paramagnetism (P), although the critical concentrations for the F–P transition strongly depend on the choice of second element. This feature has recently been explained by the authors on the basis of the finite-temperature theory of amorphous magnetic alloys [18, 19, 20]; the transition from the SG phase to ferromagnetism is caused by the enhancement of Fe local densities of states (DOS) at the Fermi level due to the decrease of average coordination number of the Fe atom via the atomic-size effect. The RSG in the Fe-rich region is realized by the thermal spin fluctuations of amplitude of Fe LMs, which violate the detailed balance between the short-range ferromagnetic interactions and the long-range antiferromagnetic interactions.

An exception is found in amorphous Fe–Y alloys, where the sputtered Fe–Y alloys do not have the ferromagnetic phase, but show SG behaviour over the whole concentration range [1]. The SG behaviour was first attributed to a characteristic interatomic distance between nearest-neighbour Fe atoms, because the observed value of 2.54 Å beyond 67 at.% Fe [21] is close to the empirical critical value 2.5 Å at which the magnetic couplings between Fe LMs change from ferromagnetic to antiferromagnetic couplings [22]. Later, Croat [2], Ishio *et al* [3], and Tange *et al* [4, 5] found that the melt-spun Fe–Y alloys show ferromagnetism at finite Y concentrations, with the maximum of Curie temperatures (T_C) at about 270 K around 80 at.% Fe. RSG behaviour has also been found recently by Tange *et al* [4, 5] for the range 50–80 at.% Fe, which is very similar to that for the other Fe-rich amorphous alloys shown in figure 1. Moreover, Fukamichi [23] observed the appearance of ferromagnetism when the sputtered Fe–Y alloys were annealed.

The experimental results mentioned above reveal that the magnetic properties of amorphous Fe–Y alloys are extremely sensitive to the different preparation conditions, which may cause changes in electronic structure, and spin fluctuations, as well as a distribution of magnetic interactions via structural and configurational disorders. Therefore, more

detailed investigations, in particular concerning the influence of the degree of disorder, are indispensable if one aims to clearly understand the different magnetic properties of amorphous Fe–Y alloys.

To elucidate the mechanism of the magnetism in amorphous Fe–Y alloys, we investigate in more detail, in this paper, various magnetic properties of amorphous Fe–Y alloys on the basis of the finite-temperature theory [18]. Moreover, we study the influence of the degree of disorder in this system and explain the difference in magnetic phase diagram between the melt-spun and the sputtered Fe–Y alloys from the viewpoint of the atomic short-range-order (ASRO) effect.

We first review in the next section the finite-temperature theory for amorphous magnetic alloys. Then, we investigate in section 3 various magnetic properties and the electronic structure of amorphous Fe–Y alloys in the most random atomic configuration, and clarify the differences between and the similarities of the magnetism behaviours exhibited by Fe–Y and Fe–Zr alloys. The latter has been regarded as a prototype of Fe-rich amorphous alloys containing early transition metals and rare-earth metals [13].

We present in subsection 3.1 the spin-polarized local DOSs, which show a double-peak structure in the Fe-rich region and a Lorentz-like structure in the Y-rich region at the Fe site. The calculated concentration dependences of various LMs and the broad distributions of LMs are presented in subsection 3.2. They are discussed from the viewpoint of electronic structure. Subsection 3.3 is devoted to the temperature variations of LMs and susceptibilities. The SG for concentrations near that of amorphous pure Fe, the RSG behaviour at around 86.5 at.% Fe, and the ferromagnetism at finite Y concentrations are found there. The calculated magnetic phase diagram for the most random atomic configuration is presented in subsection 3.4. A SG–F–P transition is found with decreasing Fe concentration, which explains qualitatively the behaviour of the melt-spun Fe–Y amorphous alloys. To clarify the origin of the two kinds of magnetic phase diagram for amorphous Fe–Y alloys shown in figure 1, the ASRO effects on the magnetization and the Curie temperatures are investigated in subsection 3.5. A phase transition from the F to the SG regime is found in the Fe-rich region when the number of Fe–Fe neighbouring pairs increases. This may explain the fact that a single SG phase is found for sputtered Fe–Y alloys. The conclusions are given in section 4. The preliminary results of this paper were reported in the proceedings of the *International Conference on Magnetism*, held in 1994 [24].

2. Theory for amorphous magnetic alloys at finite temperatures

We consider the binary amorphous alloys described by the degenerate-band Hubbard model with Hund's rule coupling, and take into account the thermal spin fluctuations by means of the functional integral method [25, 26, 27]. The interacting electron system is, then, transformed into a one-electron system with time-dependent fictitious fields acting on each site. Within the static and molecular-field approximations [28, 29, 30], the thermal average of the LM for atom α on site 0 is given in a classical form as follows [18, 31]:

$$\langle m_0 \rangle = \int \mathrm{d}\xi \ \xi \mathrm{e}^{-\beta \Psi_0(\xi)} \Big/ \int \mathrm{d}\xi \ \mathrm{e}^{-\beta \Psi_0(\xi)} \tag{1}$$

$$\Psi_0(\xi) = E_0(\xi) + \sum_{j \neq 0} \Phi_{0j}^{(a)}(\xi) - \sum_{j \neq 0} \Phi_{0j}^{(e)}(\xi) \frac{\langle m_j \rangle}{x_j} \ . \tag{2}$$

Here β is the inverse temperature. The field variable ξ can be regarded as an adiabatic LM on site 0 according to equation (2). The energy $\Psi_0(\xi)$ consists of the single-site energy

functional on site 0 ($E_0(\xi)$), the atomic pair energy between sites 0 and j ($\Phi_{0j}^{(a)}(\xi)$), and the exchange pair energy ($\Phi_{0j}^{(e)}(\xi)$) between the central LM ξ and the neighbouring LM $\langle m_j \rangle$ with average amplitude x_j.

The central LM $\langle m_0 \rangle$ is then given by the surrounding LM $\{\langle m_j \rangle\}$, the coordination number z, the atomic configuration $\{\gamma_j\}$, the squares of transfer integrals $\{y_j = t_{0j}^2\}$ for amorphous pure metals, the effective medium $\mathcal{L}_\sigma$ for electrons describing the effects of random potentials and the thermal spin fluctuations in the energies $E_0(\xi)$, $\Phi_{0j}^{(a)}(\xi)$, and $\Phi_{0j}^{(e)}(\xi)$, and the effective self-energy $\mathcal{S}_\sigma$ describing the structural disorder outside the NN shell (see [18] for further details). These variables randomly change in amorphous alloys. Therefore, we treat them by introducing the distribution function $g_\alpha(\langle m_j \rangle)$ for the LM of atom α, the distribution $p_\alpha(z)$ for the coordination number of atom α, the probability $p^{\alpha\alpha}$ of finding an atom of type α on the NN site of the central atom α, and the distribution $p_s(y_j)$ for squares of the transfer integrals. Since the distribution for the central LM $g_\alpha(\langle m_0 \rangle)$ obtained from equation (2) should be identical to those for the neighbouring LMs $g_\alpha(\langle m_j \rangle)$, we obtain an integral equation for the distribution of LMs as follows:

$$g_\alpha(M) = \sum_z p_\alpha(z) \sum_{n=0}^z \Gamma(n, z, p^{\alpha\alpha}) \int \delta(M - \langle m_\alpha \rangle)$$

$$\times \prod_{i=1}^n \left[p_s(y_i)\, dy_i\, g_\alpha(m_i)\, dm_i \right] \prod_{j=n+1}^z \left[p_s(y_j)\, dy_j\, g_{\bar\alpha}(m_j)\, dm_j \right]. \tag{3}$$

We adopt here a simple form for the distribution $p_\alpha(z)$:

$$p_\alpha(z) = (z_\alpha^* - [z_\alpha^*])\delta_{z[z_\alpha^*]+1} + ([z_\alpha^*] + 1 - z_\alpha^*)\delta_{z[z_\alpha^*]}$$

where [ ] is Gauss's notation, so that the average coordination number

$$z_\alpha^* = \sum_z p_\alpha(z)z$$

is described correctly. $\Gamma(n, z, p^{\alpha\alpha})$ in equation (3) is a binomial distribution function given by

$$\Gamma(n, z, p^{\alpha\alpha}) = (p^{\alpha\alpha})^n (1 - p^{\alpha\alpha})^{z-n} z!/n!(z-n)!$$

in which $p^{\alpha\alpha}$ is written in terms of Cowley's ASRO parameter τ_α and concentration c_α as $p^{\alpha\alpha} = c_\alpha + (1 - c_\alpha)\tau_\alpha$. Note that the suffix α denotes the type of atom on the central site.

Making use of the decoupling approximation for both $p_s(y_j)$ and $g(m_j)$ on the right-hand-side of equation (3), which is correct up to the second moments, we reach the final expression for the self-consistent equations for the average LM $\left[[\langle m_\alpha \rangle]_s\right]_c$ of atom α and the SG order parameter $\left[[\langle m_\alpha \rangle^2]_s\right]_c$ as follows:

$$\begin{bmatrix} \left[[\langle m_\alpha \rangle]_s\right]_c \\ \left[[\langle m_\alpha \rangle^2]_s\right]_c \end{bmatrix} = \int \begin{bmatrix} M \\ M^2 \end{bmatrix} g_\alpha(M)\, dM$$

$$= \sum_z p_\alpha(z) \sum_{n=0}^z \Gamma(n, z, p^{\alpha\alpha}) \sum_{i=0}^n \Gamma\left(i, n, \frac{1}{2}\right) \sum_{j=0}^{z-n} \Gamma\left(j, z-n, \frac{1}{2}\right)$$

$$\times \sum_{k_1=0}^i \Gamma(k_1, i, q_\alpha) \sum_{k_2=0}^{n-i} \Gamma(k_2, n-i, q_\alpha) \sum_{l_1=0}^j \Gamma(l_1, j, q_{\bar\alpha})$$

$$\times \sum_{l_2=0}^{z-n-j} \Gamma(l_2, z-n-j, q_{\bar\alpha}) \begin{bmatrix} \langle \xi_\alpha \rangle(z, n, i, j, k_1, k_2, l_1, l_2) \\ \langle \xi_\alpha \rangle(z, n, i, j, k_1, k_2, l_1, l_2)^2 \end{bmatrix} \tag{4}$$

$$q_\alpha = \frac{1}{2}\left[1 + \frac{\big[[\langle m_\alpha \rangle]_s\big]_c}{\big[[\langle m_\alpha \rangle^2]_s\big]_c^{1/2}}\right]. \tag{5}$$

Here $[\ \ ]_s$ ($[\ \ ]_c$) denotes the structural (configurational) average, and

$$\langle \xi_\alpha \rangle(z, n, i, j, k_1, k_2, l_1, l_2) = \int d\xi\ \xi e^{-\beta\Psi_\alpha(\xi,z,n,i,j,k_1,k_2,l_1,l_2)} \Big/ \int d\xi\ e^{-\beta\Psi_\alpha(\xi,z,n,i,j,k_1,k_2,l_1,l_2)} \tag{6}$$

where

$$
\begin{aligned}
\Psi_\alpha(\xi, z, n, i, j, k_1, k_2, l_1, l_2) &= E_\alpha(\xi, z, i+j) + i\Phi^{(a)}_{\alpha\alpha+}(\xi, z, i+j) \\
&\quad + (n-i)\Phi^{(a)}_{\alpha\alpha-}(\xi, z, i+j) + j\Phi^{(a)}_{\alpha\bar\alpha+}(\xi, z, i+j) \\
&\quad + (z-n-j)\Phi^{(a)}_{\alpha\bar\alpha-}(\xi, z, i+j) \\
&\quad - \left[(2k_1 - i)\Phi^{(e)}_{\alpha\alpha+}(\xi, z, i+j) + (2k_2 - n + i)\Phi^{(e)}_{\alpha\alpha-}(\xi, z, i+j) \right] \\
&\quad \times \frac{\big[[\langle m_\alpha \rangle^2]_s\big]_c^{1/2}}{[x_\alpha]_s} - \left[(2l_1 - j)\Phi^{(e)}_{\alpha\bar\alpha+}(\xi, z, i+j) + (2l_2 - z + n + j) \right. \\
&\quad \times \left. \Phi^{(e)}_{\alpha\bar\alpha-}(\xi, z, i+j) \right] \frac{\big[[\langle m_{\bar\alpha} \rangle^2]_s\big]_c^{1/2}}{[x_{\bar\alpha}]_s}.
\end{aligned}
\tag{7}
$$

In equation (7), the subscripts $+$ and $-$ denote the contracted ($[R]_s - [(\delta R^2)]_s^{1/2}$) and stretched ($[R]_s + [(\delta R^2)]_s^{1/2}$) pairs for interatomic distance R.

In the present method, the structural disorder in the transfer integrals $\{t_{0j}\}$ in a cluster is described by the number i (j) of contracted atoms α ($\bar\alpha$) among n ($z-n$) atoms of type α ($\bar\alpha$) via the fluctuation of the interatomic distance ($[(\delta R^2)]_s^{1/2}/[R]_s$), and the spin configuration on the NN shell is described by the number k_1 (l_1) of up spins among the i (j) contracted atoms α ($\bar\alpha$) and the number k_2 (l_2) of up spins among the $n-i$ ($z-n-j$) stretched atoms α ($\bar\alpha$). The effective media $\mathcal{L}_\sigma$ and $\mathcal{S}_\sigma$ are obtained by solving the self-consistent CPA (coherent-potential approximation) and Bethe-type equations (see equations (49) and (82) in [18]), in which we need the average DOS for amorphous pure metals.

The atomic-size effect is taken into account via the average coordination number z_α^*, which is given by

$$z_\alpha^* = z_\alpha^*(0) + p^{\alpha\alpha}[z_\alpha^*(1) - z_\alpha^*(0)]. \tag{8}$$

Here the average coordination numbers $z_\alpha^*(0)$ and $z_\alpha^*(1)$ are the values for $p^{\alpha\alpha} = 0$ and $p^{\alpha\alpha} = 1$, respectively, which are estimated approximately from the model of dense random packing of hard spheres (DRPHS; see appendix B in [18]). This relationship means that the coordination number of an atom with larger atomic size increases linearly with decreasing number of the same type of neighbouring atoms. It should be noted that the atomic-size effect causes $\tau_\alpha \neq \tau_{\bar\alpha}$ because of the sum rule for the α–$\bar\alpha$ pair:

$$z_\alpha^*(1 - \tau_\alpha) = z_{\bar\alpha}^*(1 - \tau_{\bar\alpha}). \tag{9}$$

We determine these parameters from the condition for the most random atomic configuration (see appendix A in [18]):

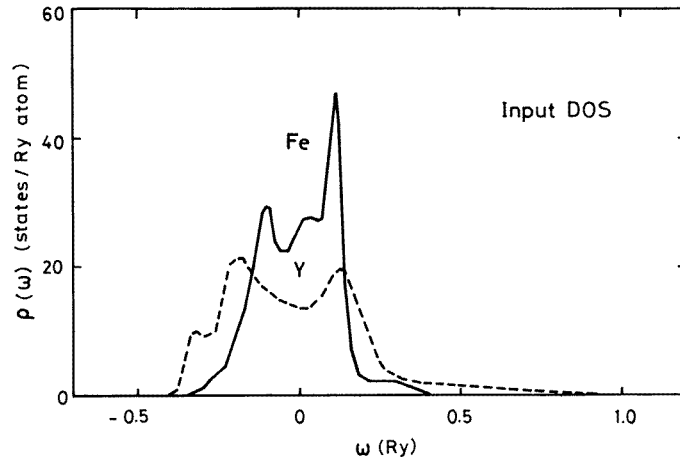$$c_\alpha \tau_{\bar\alpha} + c_{\bar\alpha} \tau_\alpha = 0. \tag{10}$$

Figure 2. The input densities of states (DOSs) for amorphous Fe [33] (solid curve) and amorphous Y (dashed curve). The latter is obtained from that of amorphous Zr [18] by scaling its bandwidth.
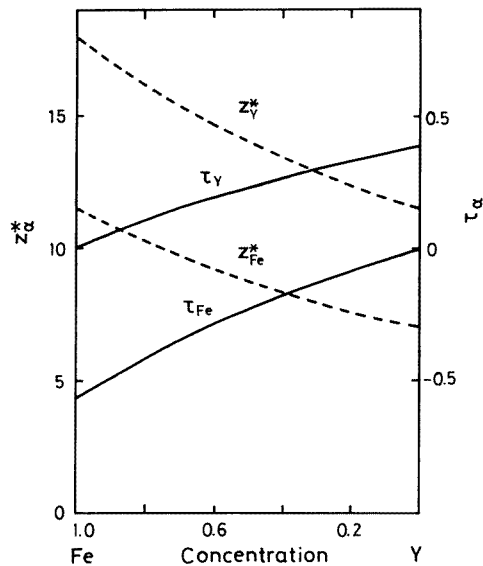

Figure 3. The concentration dependence of the atomic short-range-order parameters $\{\tau_\alpha\}$ (solid lines) and the average coordination numbers $\{z_\alpha^*\}$ (dashed lines), which are obtained from the condition for the most random atomic configuration (equation (10)) and equation (8), where $z_{\mathrm{Fe}}^*(0) = 7.0$, $z_{\mathrm{Y}}^*(0) = 18.0$, and $z_{\mathrm{Fe}}^*(1) = z_{\mathrm{Y}}^*(1) = 11.5$.

3. Numerical results

3.1. Choice of parameters and densities of states

The theory contains several parameters describing the amorphous and electronic structures in binary amorphous alloys. We adopt the same input DOS for amorphous Fe [33] as

used in the calculations for amorphous Fe and Fe–Zr alloys [14, 15, 18, 20]. The DOS for amorphous Y is obtained from that of amorphous Zr [32] by scaling its bandwidth with the same ratio as in their fcc counterparts (i.e. $W_Y^{amor} = W_{Zr}^{amor} W_Y^{fcc}/W_{Zr}^{fcc}$) (see figure 2). The d-electron number and effective exchange energy parameter for amorphous Fe are chosen to be the same values as those for amorphous Fe–Zr alloys [15, 18, 20]: $n_{Fe} = 7.0 + (1 - c_{Fe}) \times 0.5$ and $\tilde{J}_{Fe} = 0.064$ Ryd; while those for amorphous Y are chosen as $n_Y = 1.7$ and $\tilde{J}_Y = 0.048$ Ryd. The latter is taken from Janak's calculation [34]. The choice of d-electron numbers has been discussed in our previous paper [18]. The fluctuation of interatomic distance ($[(\delta R^2)]_s^{1/2}/[R]_s$) is chosen as 0.06 which is estimated from both experimental [35] and calculated [36] pair distribution functions for amorphous Fe. We first adopt the ASRO parameters $\{\tau_\alpha\}$ determined from the most random atomic configuration (see equation (10)). The large difference in atomic size between Fe and Y atoms is taken into account: $z_{Fe}^*(0) = 7.0$, $z_Y^*(0) = 18.0$, $z_{Fe}^*(1) = z_Y^*(1) = 11.5$. The values of $\{\tau_\alpha\}$ and $\{z_\alpha^*\}$ are shown in figure 3.
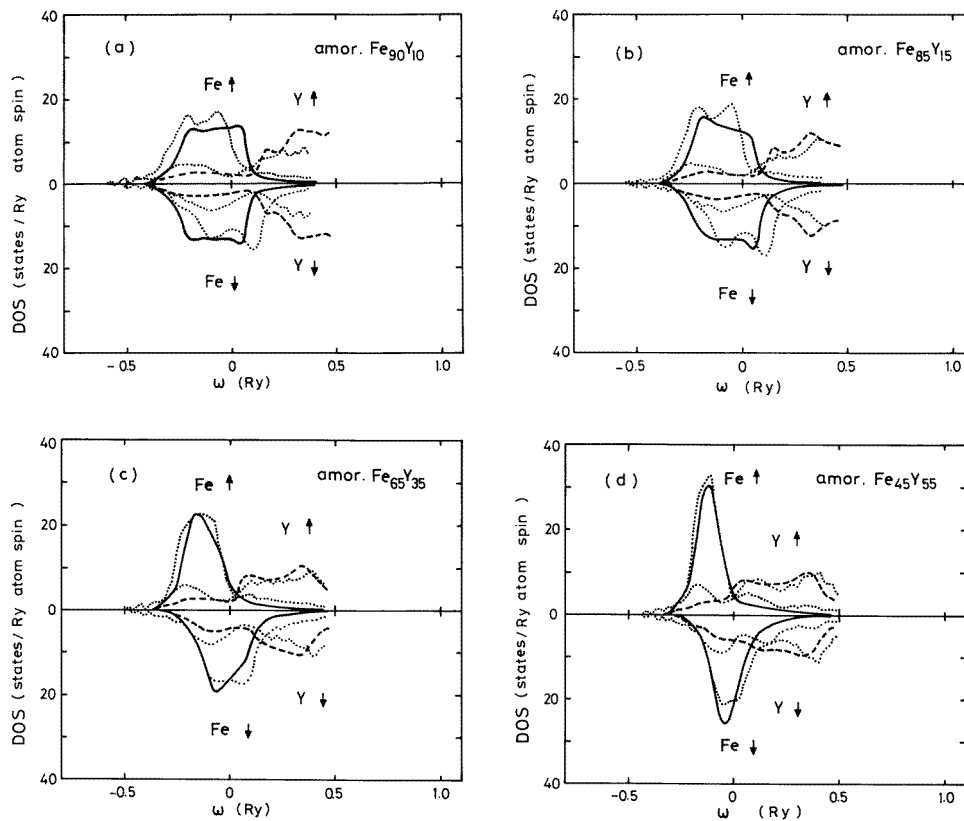

Figure 4. Calculated spin-polarized local densities of states (DOSs) of amorphous Fe–Y alloys in the most random atomic configuration at 75 K. The results for the ground state obtained from the supercell approach are represented by dotted curves; (a) $c_{Fe} = 0.89$, (b) $c_{Fe} = 0.83$, (c) $c_{Fe} = 0.67$, (d) $c_{Fe} = 0.48$ [37].

We illustrate in figure 4 the spin-polarized local DOS calculated in the most random atomic configuration at 75 K. The Fe 3d bands beyond 87 at.% Fe in amorphous Fe–Y alloys hybridize less with Y 4d bands as compared with those in amorphous Fe–Zr alloys [18].

With decreasing Fe concentration, the bandwidth of the Fe local DOS gradually narrows, and the local DOS polarizes with the appearance of ferromagnetism (see figures 4(b), (c)). The down-spin bandwidth for the Fe local DOS is larger than the up-spin one, due to there being more mixing of electrons between Fe and Y sites. More mixing of 4d state with 3d states in the down-spin band also gives rise to more electrons with down spin below the Fermi level on Y sites and leads to a formation of negative moments on Y sites. With further decrease of the Fe concentration, the band splitting of the Fe local DOS decreases gradually because of there being more holes in the up-spin 3d electrons above the Fermi level due to hybridization with 4d electrons on Y sites. Below 50 at.% Fe, the Fe local DOSs form a Lorentz-like narrow band located in the broad Y band, as seen from figure 4(d). Comparing these results with the local DOS in amorphous Fe–Zr alloys (see figure 3 in [18]), we find that the Fe local DOSs in amorphous Fe–Y alloys show narrower bandwidth in particular below 65 at.% Fe because of less hybridization with 4d electrons, which makes amorphous Fe–Y alloys more polarizable together with a larger value of $\tilde{J}_Y$.
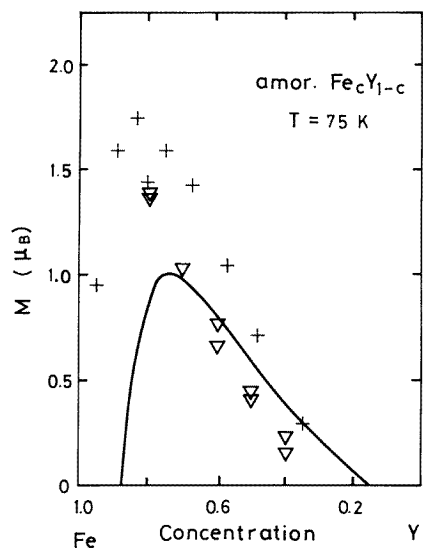

Figure 5. The calculated magnetization $[[\langle m \rangle]_s]_c$ versus concentration curve for the most random atomic configuration at 75 K. Experimental data for the saturated magnetization of the melt-spun Fe–Y alloys are shown by inverted triangles ($\triangledown$) [5]. The crosses show the results for the ground state obtained from the supercell approach [37].
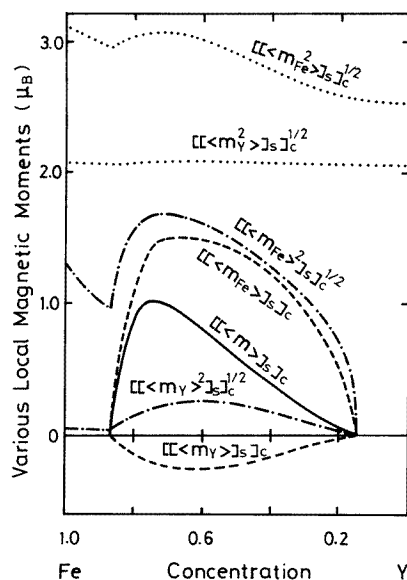
Figure 6. The concentration dependences of various local moments for the most random atomic configuration at 75 K: $[[\langle m \rangle]_s]_c$ (solid curve), $[[\langle m_\alpha \rangle]_s]_c$ (dashed curve), $[[\langle m_\alpha \rangle^2]_s]_c^{1/2}$ (dot–dashed curves), and $[[\langle m_\alpha^2 \rangle]_s]_c^{1/2}$ (dotted curves).

It is found that our results for spin-polarized DOSs with the most random atomic configuration reproduce well those obtained from the supercell approach [37] (dashed curves in figure 4). This supports the validity of the finite-temperature theory. A serious difference is found beyond 90 at.% Fe, because of the small unit cell in the supercell approach, as we have discussed in recent papers [15, 18].

3.2. The concentration dependence of various local moments

We have numerically investigated the concentration dependence of magnetic properties in the most random atomic configuration. Figure 5 shows the calculated magnetization ($[[\langle m \rangle]_s]_c$) versus concentration curve at 75 K. The result explains qualitatively the experimental data for the saturated magnetization of the melt-spun Fe–Y alloys [5] as shown by inverted triangles in figure 5. In our calculations, a net magnetization appears below 87 at.% Fe and shows a maximum of 1.0 μ_B at around 73 at.% Fe. With further decrease of the Fe concentration, the magnetization gradually decreases until 15 at.% Fe is reached where the paramagnetism appears.

The appearance of ferromagnetism is attributed to the large difference in atomic size between Fe and Y atoms; as the Y concentration increases, small Fe atoms on the NN shell of an Fe atom are replaced by large Y atoms, so the average coordination number z^*_{Fe} is reduced according to the DRPHS model. This leads to a change in electronic structure via the transfer integrals $\{t_{0j}\}$. We have examined the nonmagnetic DOS at 65 at.% Fe in the most random atomic configuration, comparing it with those DOSs in which $z^*_\alpha = 11.5$ ($\alpha = $ Fe and Y). We found that the former shrinks the bandwidth of the Fe local DOS and enhances the local DOS at the Fermi level. These effects produce a magnetic energy gain, so the ferromagnetism appears. In fact, we have calculated the magnetization keeping the average coordination number $z^*_\alpha = 11.5$, and found no net magnetization over the whole concentration range. This mechanism is the same as that in amorphous Fe–Zr alloys [18], although the net magnetization in amorphous Fe–Y alloys is enhanced by 0.1 μ_B as compared with that in amorphous Fe–Zr alloys [20, 24]. The SG–F transition is therefore a characteristic of amorphous Fe early-transition-metal alloys. Recent *ab initio* calculations by Becker and Hafner using the supercell approach [37] have also found a reduction of the coordination number of Fe with decreasing Fe concentration, in agreement with our results for the most random atomic configuration.

The disagreement between our result and that obtained by Becker and Hafner beyond 90 at.% Fe is attributed to the small number of atoms (64 atoms) in a unit cell in the supercell approach and the periodic boundary condition for magnetic structure with the same unit cell as in the crystalline structure. The former is not sufficient for describing competing systems such as the SG because of the small energy difference between various spin configurations. The latter generally overestimates the magnetization in the competing systems.

Various LMs also show a concentration dependence similar to those in amorphous Fe–Zr alloys [20] as shown in figure 6. But Fe LMs are enhanced because of there being less hybridization between Fe 3d and Y 4d orbitals, and the Y LMs are decreased in magnitude because $n_Y < n_{Zr}$, as compared with those for the amorphous Fe–Zr alloys (see subsection 3.1).

Calculated distribution functions $g(M)$ $(= \sum_\alpha c_\alpha g_\alpha(M))$ at various concentrations are presented in figure 7. The narrow peak at the centre is mainly contributed by the small Y LMs, while the very broad peak in the positive region comes from the large fluctuations of Fe LMs due to the structural and configurational disorder. When Fe concentration increases beyond 75 at.% Fe, negative Fe LMs appear. Then, the broad peak flattens and extends to the negative region. This is caused by the appearance of nonlinear magnetic couplings and the effect of the local environment on the amplitude of the LMs. Further increase of Fe concentration results in the SG behaviour which is characterized by a symmetric and very broad distribution from -2.6 μ_B to 2.6 μ_B.

Becker and Hafner [37] have calculated the distribution functions for the ground state on the basis of the supercell method (see the inset of figure 7). They also found a large
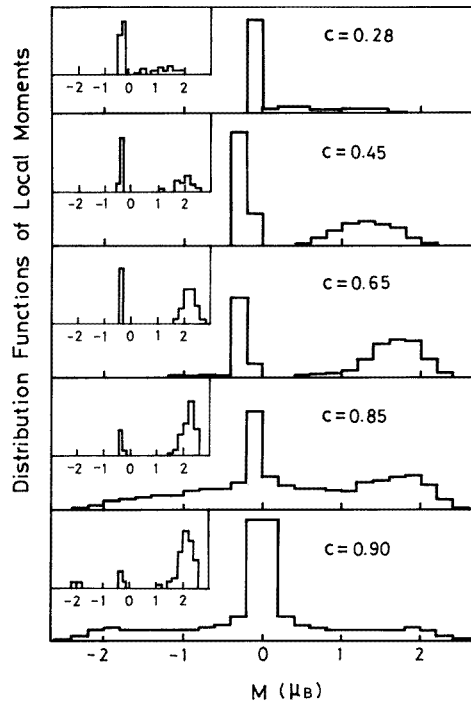
Figure 7. Distribution functions $g(M)$ for various Fe concentrations calculated for the most random atomic configuration at 75 K. The insets show the results for the ground state obtained from the supercell approach for $c_{Fe} = 0.35, 0.48, 0.67, 0.83, 0.89$ from the top to the bottom [37].

number of negative Fe LMs beyond 80 at.% Fe and attributed the appearance of negative Fe LMs to the competing exchange interactions which are traced back to both fluctuations in the local charge densities and bonding properties related to the number of contracted atoms on the NN shell. This explains the decrease of magnetization in the Fe-rich region in their results (see the crosses in figure 5). It is, however, found that the results still lead to a finite value of magnetization in pure Fe as found in their calculations for amorphous Fe–Zr alloys [38], because of the small unit cell with periodic boundary conditions in the supercell approach [15, 18].

3.3. Temperature variations of magnetic moments and susceptibilities

We have calculated the temperature dependence of the magnetization, SG order parameter, and spin susceptibility in the most random atomic configuration at various concentrations. The results are illustrated in figures 8 and 9. As shown in figure 8(a), the SG solution appears beyond 87 at.% Fe, and the spin susceptibility shows a cusp at T_g [1]. The inverse susceptibility exhibits upward convexity above T_g as shown in figure 9, as was observed by Fukamichi for $Fe_{92.5}Y_{7.5}$ amorphous alloy [23]. This behaviour is related to the close-packed structure, because it has also been found theoretically in amorphous Fe [39], amorphous Fe–Zr alloys [20] and fcc Fe–Ni alloys [40].

In the narrow region around 86.5 at.% Fe, we found RSG behaviours as shown in figure 8(b). The net magnetization appears in a temperature range of 160–50 K, while the
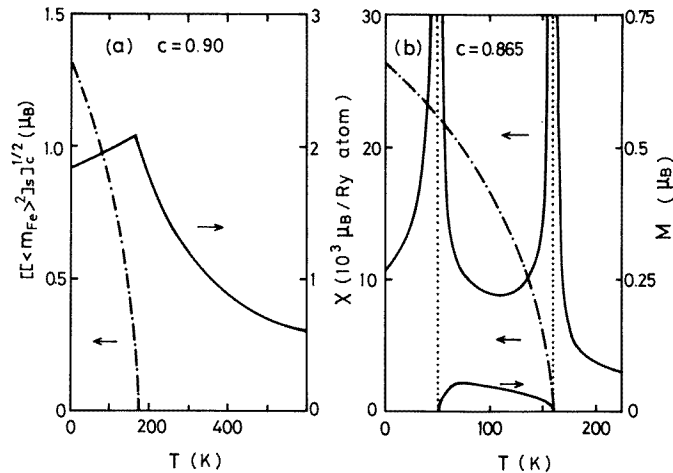
Figure 8. The temperature dependences of the magnetization (solid curve), SG order parameter (dot–dashed curves), and spin susceptibility (solid curves) for amorphous $Fe_{90}Y_{10}$ alloy (a), and $Fe_{86.5}Y_{13.5}$ alloy (b). The vertical dotted lines denote the critical temperatures.
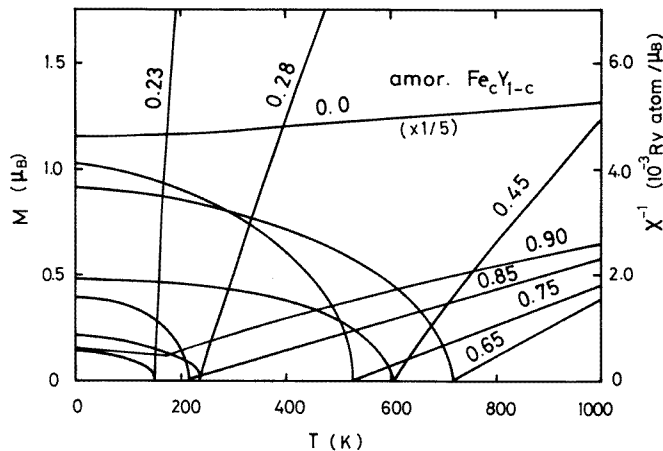

Figure 9. The temperature dependences of the magnetization and inverse spin susceptibilities at various Fe concentrations. Note that the curve for the inverse spin susceptibility at $c_{Fe} = 0.0$ is multiplied by 1/5.

SG order parameter increases gradually below 50 K. These behaviours have been observed for the melt-spun Fe–Y alloys [4], but the RSG region extends over the whole concentration range in the experimental data, contradicting the present result for the most random atomic configuration. The competing interactions between more distant LMs, which are not fully taken into account in the present calculations, may explain the data.

In the present calculations, ferromagnetism is found below 86 at.% Fe. The calculated magnetization versus temperature curves are close to the Brillouin type (see figure 9). The inverse susceptibilities, on the other hand, obey the Curie–Weiss law above T_C in the Fe-rich region, but begin to bend and rapidly decrease at low temperatures below 50 at.% Fe. The
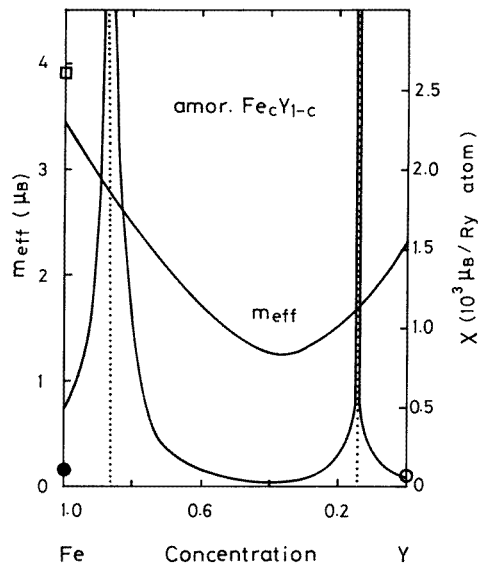
Figure 10. Effective Bohr magneton numbers m_{eff} obtained at around 1000 K and high-field spin susceptibilities at 75 K for the most random atomic configuration. The vertical dotted lines show the critical concentrations for the transitions from ferromagnetism to the spin-glass phase (at around 87 at.% Fe) and paramagnetism (at around 15 at.% Fe), respectively. The square (□) shows the experimental value of m_{eff} for liquid Fe [41], the full circle (●) shows the high-field susceptibility for bcc Fe at 4.2 K [42], and the open circle (○) shows the susceptibility for hcp Y at room temperature [43].

Pauli paramagnetic character is found only for amorphous pure Y.

The calculated effective Bohr magneton numbers m_{eff} at around 1000 K and high-field spin susceptibilities χ_{HF} at 75 K are shown in figure 10. The former is obtained from the paramagnetic inverse susceptibilities in figure 9, and the latter is obtained numerically from the change of magnetization with respect to the applied magnetic field. The effective Bohr magneton numbers have a minimum at around 35 at.% Fe and increase towards both pure limits; this is similar to the case for amorphous Fe–Zr alloys [20]. The value in the limit of amorphous pure Fe is 3.4 μ_B, being comparable to that for liquid Fe [41] (3.9 μ_B), and that in the limit for amorphous pure Y is about 2.2 μ_B. The latter is rather small as compared to that of amorphous pure Zr (5.2 μ_B [20]) because of the narrower bandwidth, stronger exchange energy parameter, and smaller d-electron number. The high-field susceptibilities χ_{HF} diverge asymmetrically at the critical concentration 87 at.% Fe corresponding to the F–SG phase transition. There are no experimental data available for χ_{HF} as far as we know. The experimental data for bcc Fe (●) at 4.2 K [42] and hcp Y (○) at room temperature [43] are presented in figure 10. The latter seems to be comparable to that of amorphous Y.

3.4. The magnetic phase diagram for the most random atomic configuration

The magnetic phase diagram obtained from the magnetization and susceptibility versus temperature curves is presented in figure 11. The most random atomic configuration leads to the three different phases: the SG, F, and P phases, depending on Fe concentration. The values of T_C obtained have a maximum of 740 K at around 60 at.% Fe, and rapidly decrease beyond 75 at.% Fe, while the values of T_g obtained increase linearly from 165 K at the
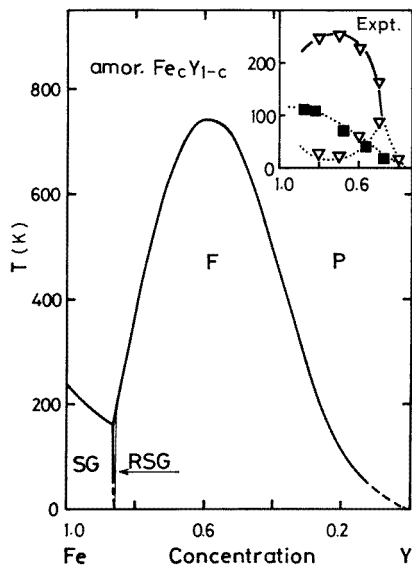
Figure 11. The calculated magnetic phase diagram for amorphous Fe–Y alloys in the most random atomic configuration showing the spin-glass (SG) phase, ferromagnetism (F), and paramagnetism (P). Re-entrant spin-glass (RSG) behaviour is found in a narrow region near the SG–F boundary. The boundaries below 50 K (dashed curves) are extrapolated. The experimental results for the melt-spun ($\triangledown$: [5]) and the sputtered ($\blacksquare$: [1]) Fe–Y alloys are shown in the inset.

triple point (86.5 at.% Fe) to 240 K for amorphous pure Fe. The result for the Fe-rich region describes qualitatively the magnetic phase diagram found for the melt-spun Fe–Y alloys [5] (see $\triangledown$ in the inset of the figure), but the calculated transition temperatures are considerably larger than the experimental data ($T_C \approx 270$ K at around 70 at.% Fe [5] and $T_g \approx 110$ K at triple points [1]). The overestimation of the transition temperatures is partly due to the molecular-field type of approximation and partly related to the ASRO effect on T_C. We will discuss the latter in the next subsection.

It should be noted that the SG below 50 at.% Fe shown in the experimental data [4, 5] has not been explained in the present calculation. Since the NN magnetic coupling between Fe LMs below 50 at.% Fe is ferromagnetic irrespective of the local environment, it is thought that more distant magnetic couplings between Fe LMs play an important role in the formation of the SG in this region.

The SG in the Fe-rich region is caused by the same mechanism as in amorphous Fe–Zr alloys [18]; the nonlinear behaviour of magnetic couplings between Fe LMs and the broad distribution of amplitude LMs due to structural disorder cause a competition between ferromagnetic and antiferromagnetic couplings, and therefore the SG. The mechanism of RSG behaviour is realized by the change of average amplitude of Fe LMs with increasing temperature, which makes the ferromagnetic coupling more favourable as we have discussed for amorphous Fe–Zr alloys [18].

3.5. Atomic short-range-order effects

It has been shown that the numerical results for the most random atomic configuration explain the appearance of the ferromagnetism at finite Y concentrations found in the melt-

spun Fe–Y alloys [4, 5]. The remaining question is that of how one describes the single SG phase found in the sputtered Fe–Y alloys [1]. The difference in magnetic phase diagram between the sputtered and melt-spun Fe–Y alloys reflects a change in local atomic structure depending on the different preparation conditions, although all of them are macroscopically regarded as amorphous structures. In the following, we will give a qualitative discussion on this problem from the theoretical point of view.
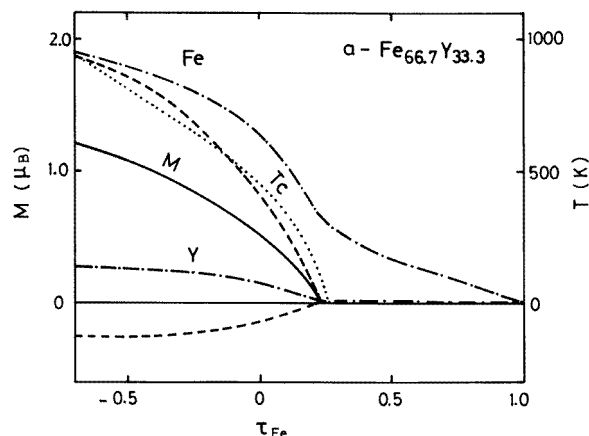

Figure 12. Magnetization (solid curve), local magnetic moments $[[\langle m_\alpha \rangle]_s]_c$ (dashed curves), and SG order parameters $[[\langle m_\alpha \rangle^2]_s]_c^{1/2}$ (dot–dashed curves) as functions of the atomic short-range-order (ASRO) parameter τ_{Fe} at 75 K. The dotted curve shows the Curie temperature versus τ_{Fe} curve.

Among various possibilities, we varied the ASRO parameter τ_α, removing the condition (10), and examined the influence of atomic configuration. Figure 12 shows our numerical results for the magnetization and T_C versus τ_{Fe} curves for amorphous $Fe_{66.7}Y_{33.3}$ alloy. We found a 17% reduction in T_C for a 10% increase of p^{FeFe}. This may partly explain the too-large T_C in the magnetic phase diagram (figure 11) as compared with the experimental values for melt-spun Fe–Y alloys [5]. Furthermore, a transition to the SG occurs in the alloy when $p^{FeFe} \gtrsim 0.75$ (i.e. $\tau_{Fe} \gtrsim 0.23$).

As shown in figure 13, the bandwidth of the Fe local DOS in the nonmagnetic state becomes broad, and a two-peak structure appears with increasing number of Fe–Fe pairs. The high-energy peak in the Fe DOS is broadened because of the hybridization between Fe 3d and Y 4d orbitals; therefore, the Fe DOS at the Fermi level is decreased with increasing p^{FeFe}. These changes in electronic structure weaken the ferromagnetism, increase the number of antiferromagnetic couplings with the band broadening because of the nonlinear magnetic couplings, and finally cause the F–SG transition at around $p^{FeFe} \approx 0.75$.

The magnetic phase diagram on the p^{FeFe}–c_{Fe} plane is obtained from the magnetization versus τ_{Fe} curves as shown in figure 14. It shows that the system could have a single SG phase in the Fe-rich region when $p^{FeFe} \gtrsim 0.8$. This may explain the SG in the sputtered Fe–Y alloys in Fe-rich region. In fact, we found that the experimental value for p^{FeFe} in the sputtered $Fe_{85}Y_{15}$ alloy [44] is about 0.845 (■ in figure 14), being above the F–SG boundary in our phase diagram. The calculated value of T_g for this alloy is about 140 K in this case ($p^{FeFe} = 0.845$), which is comparable to the experimental value of 100 K [44].

On the other hand, the appearance of the ferromagnetism found in the sputtered Fe–Y alloys after annealing [23] may also be interpreted in terms of the ASRO effect, assuming
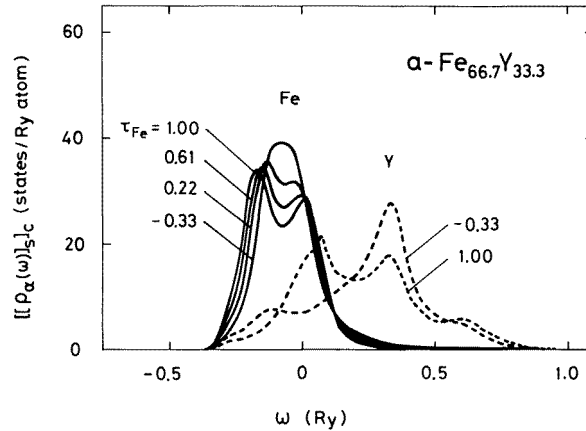
Figure 13. The local DOS $[[\rho_\alpha(\omega)]_s]_c$ (α = Fe: solid curves; Y: dashed curves) for various ASRO parameters τ_{Fe} for nonmagnetic amorphous Fe$_{66.7}$Y$_{33.3}$ alloy.
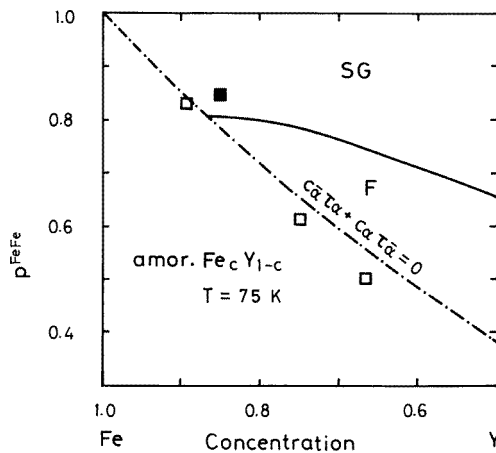

Figure 14. The calculated magnetic phase diagram on the p^{FeFe}–c_{Fe} plane at 75 K. The dot–dashed curve denotes the line for the most random atomic configuration along which figure 11 was obtained, and the solid curve denotes the phase boundary between the spin-glass (SG) phase and ferromagnetism (F). Experimental values for p^{FeFe} for the sputtered Fe$_{85}$Y$_{15}$ alloy [44] and Fe–Y compounds [45] are represented by ■ and □, respectively.

that the ASRO shifts a little toward the crystalline counterparts after annealing. Because the values of p^{FeFe} in Fe–Y compounds [45] are below the F–SG boundary (see □ in figure 14), our phase diagram explains the ferromagnetism.

4. Conclusions

We have investigated various magnetic properties of amorphous Fe–Y alloys at finite temperatures. The numerical results obtained have shown that amorphous Fe–Y alloys in the most random atomic configuration exhibit SG behaviour beyond about 90 at.% Fe, RSG behaviour at around 86.5 at.% Fe, ferromagnetism, and paramagnetism in the Y-rich

region. The results explain qualitatively the magnetic properties of the melt-spun Fe–Y alloys in the Fe-rich region, although RSG behaviour over the whole concentration range is not obtained. An overestimate of T_C by a factor of 2 was attributed partly to the deviation from the most random atomic configuration and partly to the use of the molecular-field approximation in the theory.

We have established that the SG for concentrations near that of amorphous pure Fe is caused by the nonlinear magnetic couplings between Fe LMs and the large fluctuations of the amplitude of LMs due to structural disorder. The ferromagnetism in the concentrated region is caused by the reduction of the average coordination number z_{Fe}^* due to the large difference in atomic size between Fe and Y atoms, since it leads to a band narrowing at the Fe site and a development of the local DOS at the Fermi level. The RSG behaviour near the SG–F boundary is realized by the large-amplitude fluctuations of LMs with increasing temperature.

We have shown that the Fe LMs show very broad distributions—in particular, near the critical concentration of the SG–F transition, where the susceptibilities show huge values. We predict that the effective Bohr magneton numbers will show a minimum at around 35 at.% Fe. These results are similar to those for the magnetism in amorphous Fe–Zr alloys, but the Fe–Y alloys seem to be more localized as compared with the Fe–Zr alloys because of there being less 3d–4d hybridization.

The two kinds of magnetic phase diagram for amorphous melt-spun and sputtered Fe–Y alloys have been interpreted in terms of ASRO; the single SG phase in the sputtered alloys [1] is attributed to the larger ASRO parameter τ_{Fe}, while the ferromagnetism in the melt-spun [4, 5] and annealed sputtered [23] alloys is explained by the disorder close to the most random atomic configuration and a reduction of τ_{Fe} during annealing, respectively.

As we have mentioned in the introduction, not only the degree of configurational disorder induced via the ASRO parameter, but also the degree of structural disorder induced via the fluctuations of interatomic distance are important factors dominating the magnetic properties of amorphous Fe–Y alloys. It is highly desirable to investigate such influences on the magnetic properties, constructing a theory that interpolates between crystals and amorphous alloys. More detailed information on the amorphous structure from various experiments is also desired to allow us to reach more solid conclusions.

Acknowledgments

References

[1] Coey J M D, Givord D, Liénard A and Rebouillat J P 1981 *J. Phys. F: Met. Phys.* **11** 2707
   Chappert J, Coey J M D, Liénard A and Rebouillat J P 1981 *J. Phys. F: Met. Phys.* **11** 2727
[2] Croat J J 1982 *J. Appl. Phys.* **53** 6932
[3] Ishio S, Fujikura M, Ishii T and Takahashi M 1986 *J. Magn. Magn. Mater.* **66** 236
[4] Tange H, Ikeda M, Ono T, Kamimori T and Goto M 1995 *J. Magn. Magn. Mater.* **140–144** 287
[5] Tange H 1994 private communication
[6] Hiroyoshi H and Fukamichi K 1981 *Phys. Lett.* **85**A 242; 1982 *J. Appl. Phys.* **53** 2226; 1983 *J. Magn. Magn. Mater.* **31–34** 1493
[7] Moorjani K and Coey J M D 1984 *Magnetic Glasses* (Amsterdam: Elsevier)

Coey J M D, Ryan D H and Yu Boliang 1984
J. Appl. Phys. **55** 1800
Coey J M D and Ryan D H 1984 *IEEE Trans. Magn.* **20** 1278
[8] Ryan D H, Coey J M D, Batalla E, Altounian Z and Ström-Olsen J O 1987 *Phys. Rev.* B **35** 8630
[9] Saito N, Hiroyoshi H, Fukamichi K and Nakagawa Y 1986 *J. Phys. F: Met. Phys.* **16** 911
[10] Karpe N, Rao K V, Torp B and Bøttiger J 1987 *Magnetic Properties of Amorphous Metals* ed A Hernando,
V Madurga, M C Sanchez-Trujillo and M Vazquez (Amsterdam: Elsevier) p 340
[11] Nicolaides G K and Rao K V 1993 *J. Magn. Magn. Mater.* **125** 195
[12] Wakabayashi H, Goto T, Fukamichi K, Komatsu H, Morimoto S and Ito A 1989 *J. Phys. Soc. Japan* **58** 3383
Wakabayashi H, Goto T, Fukamichi K and Komatsu H 1990 *J. Phys.: Condens. Matter* **2** 417
[13] Fukamichi K, Goto T, Komatsu H and Wakabayashi H 1989 *Proc. 4th Int. Conf. on The Physics of Magnetic
Materials (Poland)* ed W Gorkowski, H K Lachowics and H Szymczak (Singapore: World Scientific)
p 354
[14] Kakehashi Y 1991 *Phys. Rev.* B **43** 10 820
[15] Yu M and Kakehashi Y 1994 *Phys. Rev.* B **49** 15 723
[16] Kakehashi Y, Yu M and Uchida T 1995 *J. Magn. Magn. Mater.* **140–144** 251
[17] Kakehashi Y and Yu M 1994 *Phys. Rev.* B **50** 6189
[18] Yu M, Kakehashi Y and Tanaka H 1994 *Phys. Rev.* B **49** 352
[19] Yu M, Kakehashi Y and Tanaka H 1994 *Mater. Sci. Eng.* A **181/182** 856
[20] Yu M and Kakehashi Y 1996 *J. Magn. Magn. Mater.* at press
[21] Forester D W, Koon N C, Schelling J H and Rhyne J J 1979 *J. Appl. Phys.* **50** 7336
[22] Néel L 1936 *Ann. Phys., Paris* **5** 232
[23] Fukamichi K 1993 private communication
[24] Yu M and Kakehashi Y 1995 *J. Magn. Magn. Mater.* **140–144** 289
Kakehashi Y and Yu M 1995 *J. Magn. Magn. Mater.* **140–144** 263
[25] Cyrot M 1972 *J. Physique* **33** 125
[26] Hubbard J 1979 *Phys. Rev.* B **19** 2626; 1979 *Phys. Rev.* B **20** 4584; 1981 *Phys. Rev.* B **23** 5974
[27] Hasegawa H 1979 *J. Phys. Soc. Japan* **46** 1504; 1980 *J. Phys. Soc. Japan* **49** 178
[28] Wang S Q, Evenson W E and Schrieffer J R 1969 *Phys. Rev. Lett.* **23** 92
Evenson W E, Schrieffer J R and Wang S Q 1970 *J. Appl. Phys.* **41** 1199
[29] Kakehashi Y 1986 *Phys. Rev.* B **34** 3243
[30] For a review on the functional integral method, see
Morandi G, Galleani E, D'Agliano and Ratto C F 1974 *Adv. Phys.* **23** 867
Fulde P 1991 *Electron Correlations in Molecules and Solids (Springer Series in Solid State Sciences 100)*
(Berlin: Springer)
[31] Kakehashi Y and Tanaka H 1992 *J. Magn. Magn. Mater.* **104–107** 91
[32] Kakehashi Y, Tanaka H and Yu M 1993 *Phys. Rev.* B **47** 7736
[33] Fujiwara T 1985 *Nippon Butsuri Gakkaishi* **40** 209
[34] Janak J F 1977 *Phys. Rev.* B **16** 255
[35] Matsuurau M, Wakabayashi H, Goto T, Komatsu H and Fukamichi K 1989 *J. Phys.: Condens. Matter* **1**
2077
[36] Yamamoto R and Doyama M 1979 *J. Phys. F: Met. Phys.* **9** 617
[37] Becker C and Hafner J 1994 *Phys. Rev.* B **50** 3913
[38] Turek I, Becker C and Hafner J 1992 *J. Phys.: Condens. Matter* **4** 7257
[39] Kakehashi Y 1990 *Phys. Rev.* B **41** 9207
[40] Kakehashi Y 1988 *Phys. Rev.* B **38** 474
[41] Nakagawa Y 1957 *J. Phys. Soc. Japan* **12** 700
Renz I and Methfessel S 1988 *J. Physique Coll.* C8 119
[42] Stoelinga J H M, Ersdorf R G and de Vries G 1969 *Physica* **41** 457
[43] Taniguchi S, Tebble R S and Williams D E G 1962 *Proc. R. Soc.* **256** 520
[44] Fujita A 1993 private communication
[45] Buschow K H J 1977 *Rep. Prog. Phys.* **40** 1179